AIAA JOURNAL
Vol. 33, No. 11, November 1995

Dynamics of Experimentally Simulated Microbursts

Abbas Alahyari* and Ellen K. Longmire†
University of Minnesota, Minneapolis, Minnesota 55455

Laboratory-simulated microbursts are used to study the behavior of buoyancy-driven downdrafts and their associated low-altitude wind shears. The microburst flowfield is simulated by releasing an axisymmetric volume of heavy liquid into a less dense ambient surrounding and allowing it to impinge on a horizontal surface. Using particle image velocimetry, normalized horizontal and vertical velocity fields are extracted at different stages during the evolution of the flow. The leading edge of the falling fluid rolls up into a vortex ring, which then impacts on the ground and expands radially outward. After the ring impinges on the surface, unsteady adverse pressure gradients cause the low-momentum boundary layer to separate and roll up into secondary vortices just ahead of the main vortex. Interaction of the primary and secondary vortices, as well as azimuthal instabilities, can produce sharp spatial variations in velocity, especially near the surface. Particle image velocimetry results show that the largest radial velocities occur close to the surface. The radial velocities decay gradually with altitude and are very small at the height of the vortex ring core. The results are scaled to and compared with previously studied atmospheric microbursts that occurred on June 30, 1982, and July 11, 1988. The experimental data generally agree well with observed and numerically simulated microbursts. Thus, it appears that the results can be used in the development and modification of ground-based and airborne microburst detection systems.

Nomenclature

F = wind shear hazard index
g = gravitational acceleration
H_0 = initial height of microburst
Re = Reynolds number, $V_0 R_0/\nu$
R_0 = microburst length scale
r = radial distance from microburst center
T_0 = microburst time scale
u = horizontal velocity
V_A = aircraft airspeed
V_G = aircraft ground speed
V_0 = microburst velocity scale
w = vertical velocity
z = height above ground
$\Delta\rho$ = microburst density difference
Γ = circulation
ν = kinematic viscosity
ρ = density of ambient fluid
ω_θ = tangential vorticity

I. Introduction

FOR more than a decade, microbursts have been recognized as the primary factor in a number of air carrier accidents.[1-3] A microburst (or downburst) is an intense, localized downdraft of air that spreads radially outward upon its impingement on the ground. Downdrafts are typically induced by rapid evaporation of moisture, melting of hail, or precipitation drag. The divergent outflow created by a microburst produces strong winds in opposite directions. The sudden changes in the speed and direction of both horizontal and vertical winds within a microburst can create hazardous conditions for aircraft within 1000 ft of the ground, particularly during takeoff and landing.[4] The difficulty is that because of their relatively small temporal and spatial scales microbursts are not easily detectable. A better understanding of this phenomenon will lead to more efficient and more reliable detection systems and survival strategies for aircraft that encounter them.

Received Jan. 30, 1995; revision received May 26, 1995; accepted for publication May 31, 1995.

*Graduate Research Assistant, Department of Aerospace Engineering and Mechanics, 107 Akerman Hall, 110 Union Street S.E.

†Assistant Professor, Department of Aerospace Engineering and Mechanics, 107 Akerman Hall, 110 Union Street S.E. Member AIAA.

The most direct method for investigation of microbursts is through observational studies and field experiments. The Northern Illinois meteorological research on downbursts (NIMROD),[2,5] the joint airport weather studies (JAWS),[6] the classify, locate, and avoid windshear (CLAWS),[7] the microburst and severe thunderstorm (MIST),[8] and the FAA-Lincoln Laboratories operational weather studies (FLOWS)[8,9] are among the major field experiments conducted to study the behavior and characteristics of microbursts and their associated wind systems in different regions of the United States. These studies have provided significant information regarding the kinematics of microbursts and the physical processes leading to formation of small convective systems. Subsequent efforts have attempted to use this information to identify conditions favorable for microburst occurrences.[10-12] The high cost and inherent low spatial and temporal resolutions of field experiments, however, have made additional approaches necessary.

Numerical studies of downdrafts,[13,14] microburst dynamics,[15,16] thunderstorm subcloud environments,[17] and microburst sensitivity experiments[18,19] have also provided significant insight into the physics of microbursts. The numerical models have been used primarily to study the causes of microbursts and their sensitivity to environmental conditions, such as relative humidity, temperature lapse rate, precipitation type and duration, surface friction, and other microphysical processes. Several studies have shown the importance of surface friction in shaping the structure of the outflow.[15,20] Most numerical models have either neglected the effect of surface friction or included models of steady convective boundary layers, which do not necessarily represent the near-ground behavior of microbursts correctly. As a result, it is not known whether these models give complete and accurate information on the structure and the complex characteristics of the gust front.

Even the best numerical models must be validated by observation of physical events. Since complete and detailed measurements within atmospheric microbursts are not available, we use a simple laboratory model to simulate the dynamics of isolated microbursts. Although laboratory models of microbursts have been studied previously,[3,20] instantaneous measurements of their velocity fields have never been obtained. Only recently, with the use of more sophisticated optical diagnostic techniques has this become possible. We should mention other related experimental studies that have been conducted on small-scale laboratory models of gravity-driven flows. Among these are experiments conducted on buoyant vortex rings, thermals, and gravity currents.[21-26] Although these experiments provide insight into the general behavior of gravity-driven flows, such as the effect of buoyancy, development of circulation

through baroclinic vorticity generation, and the role of shear and gravitational instabilities, no single experiment contains all three important features present in downburst flows, namely, negative buoyancy, horizontal vorticity, and interaction with a horizontal surface. As a result, the findings are not directly applicable to downburst outflows.

This paper describes the dynamics of the transient flow produced by a descending mass of heavier fluid through a less dense ambient surrounding and its subsequent impingement on a horizontal surface. Our laboratory model, explained in Sec. II, is similar in principle to that used by Lundgren et al.,[20] but our investigation approach is of a more quantitative nature. The experimental facility, procedure, and the measurement technique are described in Sec. III. In Sec. IV, we discuss the evolution and the structure of the simulated flow. We then compare the scaled results with the downbursts observed on June 30, 1982, and July 11, 1988, in the Denver, Colorado, area. Although these downbursts were partially driven by condensate loading, we chose them for comparison with our model because an adequate amount of observational data exists, and they were simulated numerically using the terminal area simulation system (TASS).[15,27]

II. Model

In this experiment an isolated microburst is modeled by releasing a small axisymmetric volume of heavier fluid through a less dense ambient surrounding. The heavier fluid impinges on a horizontal plate, which represents the ground. The model displays the dynamic characteristics of atmospheric microbursts, such as the descending vortices formed at the interface between the two fluids, the divergent outflow as the heavier fluid approaches the ground, and a turbulent vortex ring embedded in a strong outflow near the ground.

Lundgren et al.[20] developed an important scaling law to relate the simulated structures to full-scale atmospheric microbursts. Assuming that the density difference $\Delta\rho$ between the two fluids is small enough for the Boussinesq approximation to hold, the inviscid equations describing the motion can be written as

$$\nabla \cdot \boldsymbol{u} = 0$$

$$\frac{d\boldsymbol{u}}{dt} = -\frac{\nabla p}{\rho} - g\frac{\rho'}{\rho}\hat{\boldsymbol{k}}$$

where ρ' is equal to $\Delta\rho$ inside the microburst and zero elsewhere. A time scale is defined as

$$T_0 = (R_0\rho/g\Delta\rho)^{\frac{1}{2}}$$

where R_0 is the spherical radius of the microburst parcel (spherical radius is defined as the radius of a sphere having the same volume). A Reynolds number is then defined as

$$Re = (V_0 R_0/\nu)$$

where V_0 is a velocity scale defined as R_0/T_0.

Lundgren et al.[20] showed that the large-scale evolution of the model microburst is Reynolds-number independent for $Re > 3000$. Therefore, by establishing the effective length and time scales for atmospheric microbursts, at sufficiently large Reynolds numbers, the model microburst can be related to its full-scale counterpart.

III. Experimental Arrangement and Procedure

A. Flow Facility

The flow is contained in a large glass tank with inner dimensions 760 × 760 × 915 mm shown schematically in Fig. 1. A raised circular plate of 610 mm diameter represents the ground. The use of this plate minimizes wall effects and also allows us to run the experiment a number of times without having to replace the tank fluid. A cylinder containing the heavier microburst fluid can be positioned at a variable height above the horizontal plate. The cylinder is open at the bottom and is drilled to a porosity of about 50% at the top. A thin latex membrane is stretched over the bottom of the cylinder, which is then filled with the heavier fluid and carefully lowered into the tank. The cylinder is submerged so that its top is a distance of at least $2R_0$ below the free surface. At the time of release, the retaining

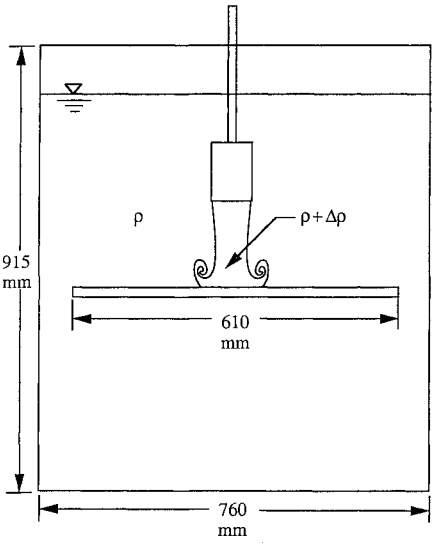

Fig. 1 Schematic of flow modeling facility.

membrane is burst by a sharp needle inside the cylinder. The needle is driven by a solenoid from above. This method of starting the flow inevitably introduces a small initial circulation. To minimize this effect, we age the membrane in an oven prior to use to make it more brittle.

The main cylindrical container used in this study has an inside diameter of 63.5 mm, a height of 87 mm, and spherical radius of 38.8 mm. A second, taller cylinder has the same inside diameter and a height of 131 mm. The spherical radius of the second cylinder is 45.2 mm. The experiments are conducted with a release height, measured from the bottom of the cylinder, of $H_0 = 3.81R_0$. This height was chosen as the baseline case because it was studied in detail by Yao.[28] Other cases have been studied, in less detail, using a release height of $H_0 = 2.86R_0$.

B. Measurement Technique

The measurement technique is double-pulsed particle image velocimetry (PIV). The flowfield is illuminated by two Nd:YAG lasers. Each laser pulses at a frequency of 10 Hz with a pulse duration of 7 ns and an energy output of approximately 200 mJ per pulse. The laser beams are converted into a thin (<1 mm) sheet of light using a 1-m focal length spherical lens and either a 19-mm or a 12.7-mm focal length cylindrical lens for vertical and horizontal sheets, respectively. Using a mirror mounted on a micrometer translation stage, the height of the horizontal sheet above the plate can be varied precisely.

Images of the flowfield seeded with TiO_2 particles are captured with a Nikon N8008s 35-mm camera equipped with a 105-mm lens. Kodak Technical Pan black and white film was found to provide the best imaging contrast. The magnification of the recording optics is 0.160 ± 0.001 for measurements in vertical planes and 0.125 ± 0.001 for measurements in horizontal planes.

To resolve directional ambiguity in the velocity field, spatial image shifting is employed by placing a rotating mirror in front of the camera lens. A galvanometer-based scanner controls the mirror motion. The mirror rotates with an angular velocity of 0.40 rad/s yielding a horizontal shift of approximately 0.2 mm on the negative.

Successful application of particle image velocimetry requires that the index of refraction of the fluids involved be matched. In this study, refractive indices were matched by using an aqueous solution of glycerol in the tank and an aqueous solution of potassium dihydrogen phosphate for the heavier downburst fluid. The experimental setup and procedure are described in more detail in Alahyari and Longmire.[29]

To extract velocity information from the images, the film negatives are digitized using a high-resolution Nikon Coolscan film scanner. Displacement vectors are measured by computing two-dimensional autocorrelations for small interrogation regions on the negative. The autocorrelation is obtained by performing a sequence of two fast Fourier transforms on the image data within each region.

In this experiment the negatives are scanned at a resolution of 1500 dpi and interrogated using 64 × 64 pixel arrays. Thus, the interrogation spots are square regions of 1 mm in dimension. These regions correspond to square grids of 6.8 and 8.6 mm in real space for measurements in vertical and horizontal planes, respectively. In the vertical cross-sectional vector fields, the bottom row of vectors corresponds to interrogation regions centered approximately 3.5 mm above the surface. The uncertainty interval associated with the velocity measurements is estimated to be $\pm 0.08 V_0$.

IV. Results

In this section, the structure and evolution of the flow for the baseline case are discussed in detail. To clarify the effects of initial release height and cylinder aspect ratio, additional cases with a lower release height and a taller cylinder are discussed. To determine how well the model resembles an actual microburst, the simulated flow is compared with two previously studied microburst events. The cases chosen for comparison are the downbursts detected on June 30, 1982, by JAWS network in the Denver, Colorado, area and the downburst on July 11, 1988, observed by the terminal Doppler weather radar (TDWR) system and also encountered by four airliners during final approach to Denver Stapleton Airport.

A. Structure and Evolution

Figure 2 shows a sequence of vertical cross sections of the velocity field through the center of a simulated microburst. Times after release for this sequence are $4.96T_0$, $6.06T_0$, and $8.26T_0$. For this case, the length scale R_0 is 0.039 m, the time scale T_0 is 0.36 s, and the velocity scale V_0 is 0.11 m/s. The initial height measured from the bottom of the cylinder is $3.81R_0$. The flow Reynolds number is 3600.

At time $T = 0$, the membrane is burst by the needle, and the heavy fluid begins to accelerate downward due to the action of gravity. As the heavy fluid descends, baroclinic vorticity develops at the interface between the two fluids. This vorticity causes the leading edge of the downdraft to roll up into a vortex ring. At $4.96T_0$ after release, the leading edge of the downdraft column is near the surface (Fig. 2a), and the horizontal vortex ring lags the leading edge by approximately $1R_0$. The ring accelerates fluid through its center and is responsible for large vertical velocities near the centerline. The largest vertical velocities at this stage are $2.3V_0$ and occur at an altitude of $1.1R_0$ above the ground. Small radial velocities are induced at the surface beneath the descending column.

In a numerical model based on inviscid vortex dynamics, Lundgren et al.[20] found that the circulation around the vortex ring develops rapidly, asymptotically approaching a constant value of

$$\Gamma = 5R_0^2/T_0$$

before the microburst reaches the surface. Using velocity fields obtained at $T/T_0 = 4.96$, we have tried to determine the total circulation contained in the experimental microburst. The circulation is estimated by evaluating the line integral of velocity along the centerline from the top of the release cylinder to the horizontal plate. Since we cannot measure the velocity within the cylinder directly, we have extrapolated the velocity profile upward to the top of the cylinder. Additional contributions to the line integral around the enclosing contour have been neglected. The estimated circulation, determined for a number of microburst events, ranges from $5R_0^2/T_0$ to $6R_0^2/T_0$. Surprisingly, this value is very similar to that found by Lundgren et al.[20]

At $T/T_0 = 6.06$, the vortex ring has reached the surface and is expanding radially outward; see Fig. 2b. Peak downward velocities are $2.5V_0$ and are located $0.7R_0$ above the surface. There is significant entrainment into the downdraft column at altitudes ranging from $0.7R_0$ to $3R_0$. At this stage, approximately one time unit after touchdown, we observe the largest horizontal velocities. In the vector field shown, the maximum horizontal velocities are $2.4V_0$. These large velocities occur near the surface and beneath the vortex core is at a distance of $1.2R_0$ from the microburst center. The leading edge of the microburst is located downstream of the vortex core at $1.7R_0$ from the microburst center. The core of the vortex is located $0.4R_0$ above the ground. The depth of the outflow is approximately $0.5R_0$.

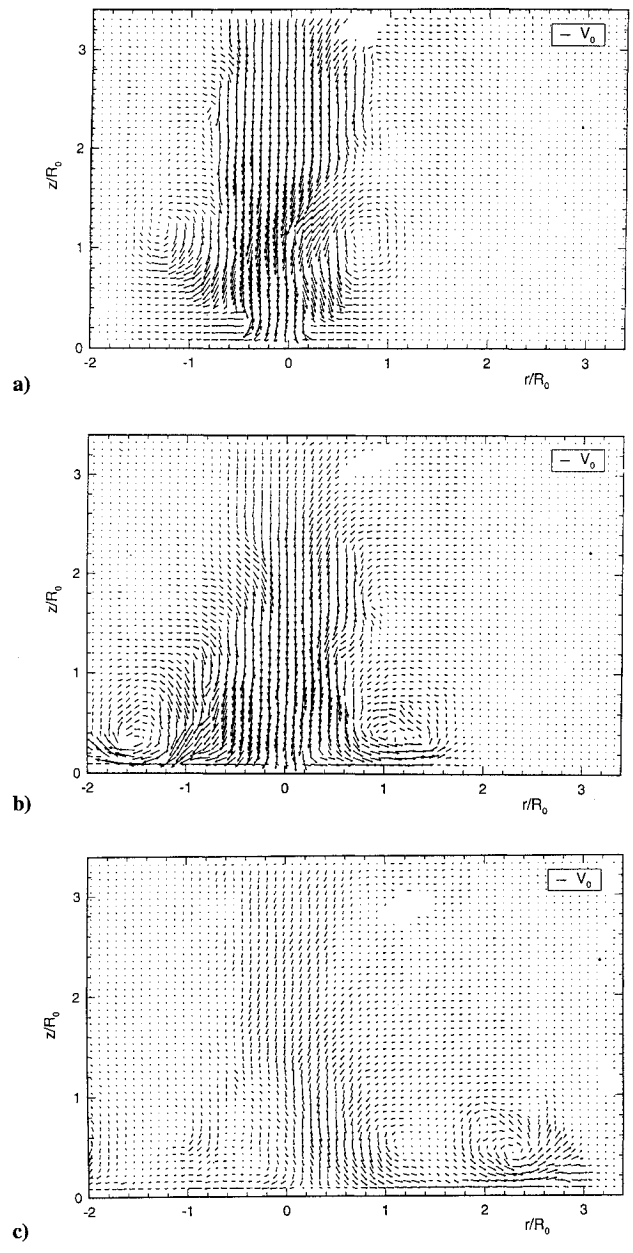

Fig. 2 Vertical cross sections of the velocity vector field; $H_0/R_0 = 3.81$, $Re = 3600$; times T/T_0 after release: a) 4.96, b) 6.06, and c) 8.26.

At $T/T_0 = 8.26$, the vortex core has expanded to a distance of $2.4R_0$ from the center, and the burst front is at a radial position of $3R_0$; see Fig. 2c. The center of the vortex remains at a height of $0.4R_0$ above the surface. The downdraft column has become disorganized, and the peak vertical velocities have decayed to approximately $0.8V_0$. These peak downward velocities are present at altitudes of 0.4–$0.7R_0$. The peak horizontal velocities, which again are associated with the ring vortex, have decayed to $1.3V_0$. Upward velocities as large as $0.7V_0$ exist at the periphery of the microburst. Also, significant downdrafts exist upstream of the vortex ring with values as high as $0.5V_0$. The propagation speed of the front between T/T_0 of 6.06 and 8.26 is about $0.5V_0$.

To obtain a better understanding of the three-dimensional behavior of the flow, velocity fields within horizontal cross sections were measured at various altitudes. The horizontal velocity fields are also advantageous, since they allow measurement of radial velocities closer to the surface. Given the thickness of the laser sheet, measurements can be made within horizontal planes as close as 1 mm ($0.025R_0$) above the surface. Figure 3 shows horizontal cross sections of the velocity field at a height of $0.05R_0$. Times after release for this sequence are $6.06T_0$ and $8.26T_0$. In Fig. 3, the origin of

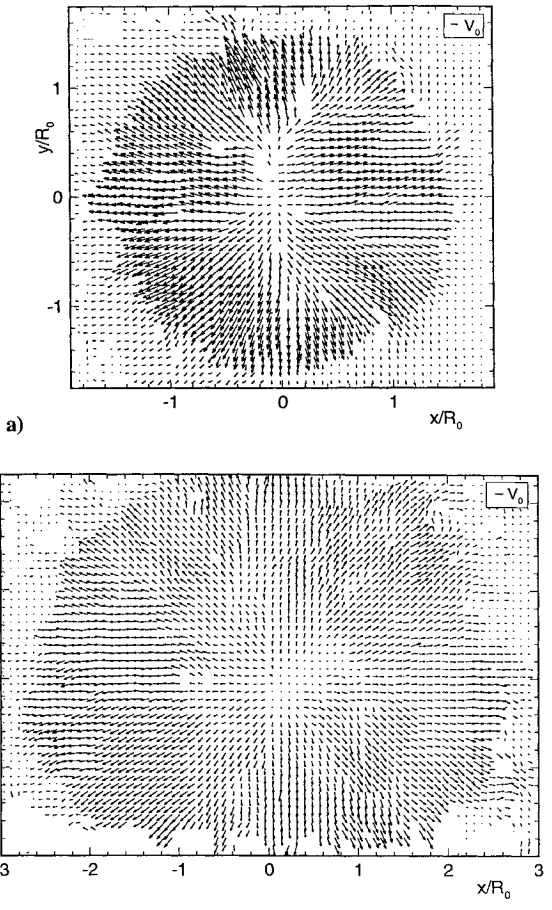

Fig. 3 Horizontal cross sections of the velocity vector field at $0.05R_0$; $H_0/R_0 = 3.81$, $Re = 3600$; times T/T_0 after release: a) 6.06 and b) 8.26.

the xy axes corresponds to the center of the release cylinder. Note that since we cannot make simultaneous measurements within both planes the sequences shown in Figs. 2 and 3 occurred within similar but separate events.

In Fig. 3a at $T/T_0 = 6.06$, the flow appears reasonably axisymmetric, but azimuthal variations and asymmetries are present. The waviness of the vortex ring is believed to be responsible for inducing azimuthal velocities and asymmetries within the field. In impulse-driven vortex rings, these instabilities have been studied by Widnall and Sullivan[30] and Saffman.[31] An additional mechanism for instability in this flow is the gravitational instability due to the presence of lighter ambient fluid near the surface overrun by the heavier downburst fluid.[25] To quantify the azimuthal variations, we have computed the rms radial and tangential velocities at each radial location. These values are a measure of variations in velocity around the circumference, not of turbulence. Typical rms values are approximately $0.4V_0$ for both velocity components. The rms for radial velocity increases sharply to values as high as $0.7V_0$ near the periphery of the burst. This behavior is typical from event to event and occurs due to the variations in the radial position of the leading edge and the presence of large velocity gradients in this region.

In Fig. 3b at $T/T_0 = 8.26$, the peak radial velocities have decayed, and the radius of peak outflow velocity has increased to $2.4R_0$. The azimuthal variations persist, although the values of the rms velocity normally decrease with time. Beyond this stage, the distance between peak outflow velocities typically scales to distances larger than 4 km and, thus, by definition, the flow is considered to be a macroburst.[32]

Figure 4 shows profiles of radial velocity at an altitude of $0.05R_0$ for several times during the evolution of a single event. Each value plotted was obtained by averaging the radial velocity around the circumference at a given radial location. The profile at $T/T_0 = 4.96$ reveals relatively small radial velocities induced by the descending downdraft column slightly before touchdown. The profiles show that the peak radial velocity occurs within one time unit after touchdown

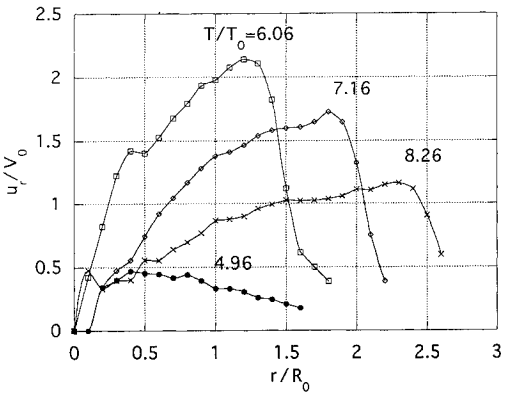

Fig. 4 Radial velocities measured at $0.05R_0$ above the plate.

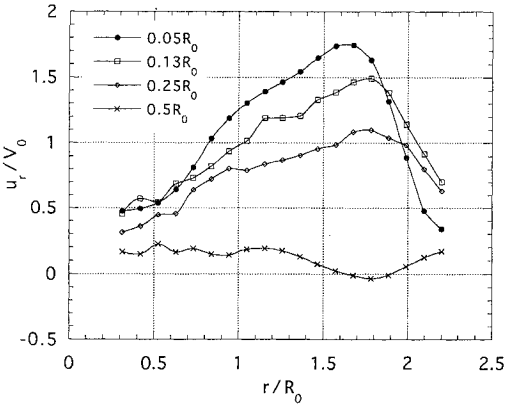

Fig. 5 Radial velocities at $T/T_0 = 7.16$ at four different heights above the surface.

and at a distance of only $1.2R_0$ from the microburst center. This behavior is consistent with hot-film measurements of radial velocity near the surface.[28] The peak average radial velocity at $T/T_0 = 6.06$ is $2.2V_0$. It should be noted, however, that since the radius of peak velocity varies around the circumference, the averaged peaks are lower than the local peak values. Velocity peaks near the leading edge of the microburst are typically $2.5V_0$, although instantaneous vectors as large as $3.1V_0$ are present. The profiles show that the peaks decay and broaden with time. Also, large radial velocities are not restricted to the region directly under the vortex core. Instead, they extend over some distance upstream. This behavior in the experiments is inconsistent with that in the numerical model presented by Lundgren et al.[20] In Lundgren's computations, the peaks in the velocity profiles remain constant and sharp for many time units after the microburst touches down. This difference, we believe, is due to the simplified friction model in the computational study. A dominant characteristic of the experimental profiles is the sharp gradient in velocity at the microburst front. The explanation for this behavior is that, in a microburst, the peak radial velocities occur close to the edge of the outflow. Also, the horizontal vorticity in the core causes the fluid to be displaced upward rather than outward. As a result, the fluid a short distance downstream of the burst is unaware of the approaching front.

In Fig. 5, profiles of radial velocity are plotted for several heights above the surface at T/T_0 of 7.16. The measurements closest to the surface (not shown) are at a height of $0.025R_0$. The measurements at this height appear to have lower peaks than those at $H = 0.05R_0$. Based on this, we estimate the thickness of the boundary layer to be approximately $0.05R_0$. Since the thickness of the laser sheet is on the same order as the boundary-layer thickness, however, we cannot determine the edge of the boundary layer with a high degree of certainty. Also, within the boundary layer, strong velocity gradients across the laser sheet may bias the measurements. In general, the largest velocities are measured at $0.05R_0$ above the surface. Above this height, the velocities decrease gradually with increasing altitude. The height of $0.5R_0$ corresponds approximately to the height

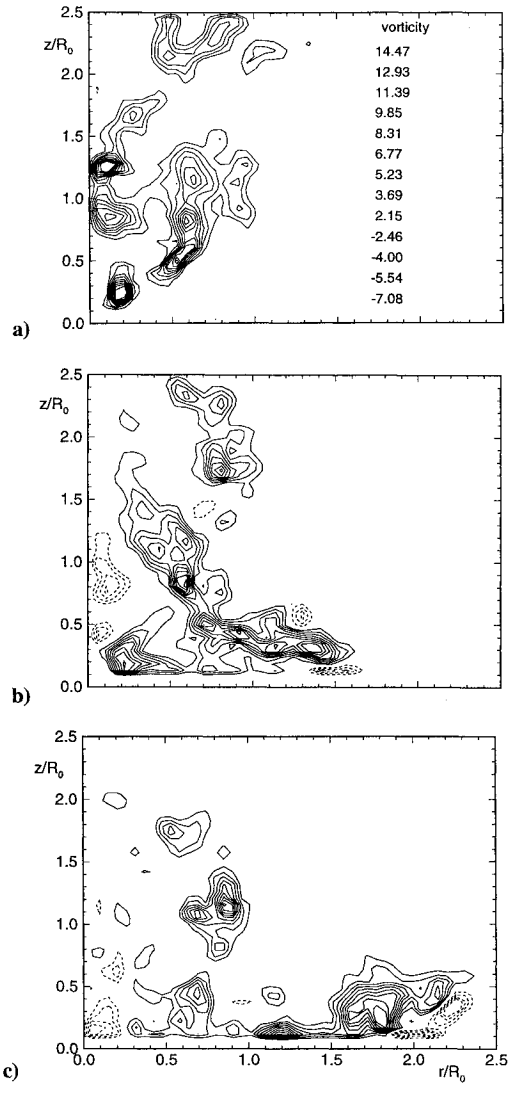

Fig. 6 Vorticity contours where dashed contours represent negative (clockwise) vorticity; times T/T_0 after release: a) 4.96, levels, b) 6.06, and c) 7.16.

of the vortex ring core. At this height, the velocity field is very disorganized, and no coherent outflow is detectable.

The interaction of the vortex ring with the no-slip horizontal surface can have complex consequences. The adverse pressure gradient downstream of the vortex ring can cause the low-momentum boundary layer formed on the surface to separate. This separated layer often rolls up into vortices with circulation opposite to that of the primary vortex. These secondary vortices have multiple effects on the evolution of the flow. Most importantly, the secondary vortices reduce the propagation velocity of the primary ring and increase the height of the outflow. The interactions between the primary and secondary vortices are similar to those observed when an impulse-driven vortex ring impinges on a surface.[33] Owing to the dominant effect of buoyancy in this study, however, the rebound of the primary ring away from the surface is much more subtle than for an impulse-driven vortex ring, and reversal of radial propagation does not occur.

To obtain additional information on these interactions, we have computed vorticity fields from the velocity measurements in vertical planes. The out-of-plane component of vorticity ω_θ given by

$$\omega_\theta = \frac{\partial w}{\partial r} - \frac{\partial u_r}{\partial z}$$

is found at each point by evaluating the line integral of velocity using the eight surrounding points.

Figure 6 shows vorticity fields calculated from velocity data at T/T_0 of 4.96, 6.06, and 7.16 for the microburst in Fig. 2. Peak

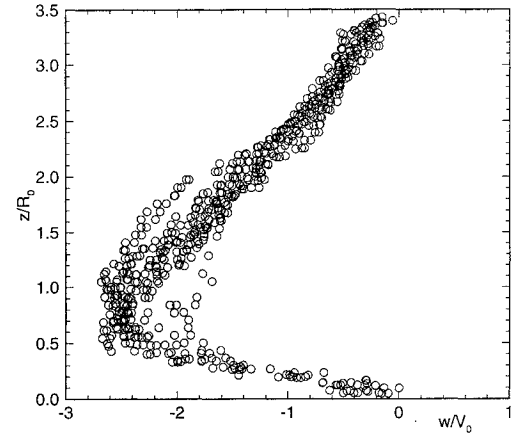

Fig. 7 Vertical velocity from the two columns closest to the centerline in the baseline case, seven events overlaid.

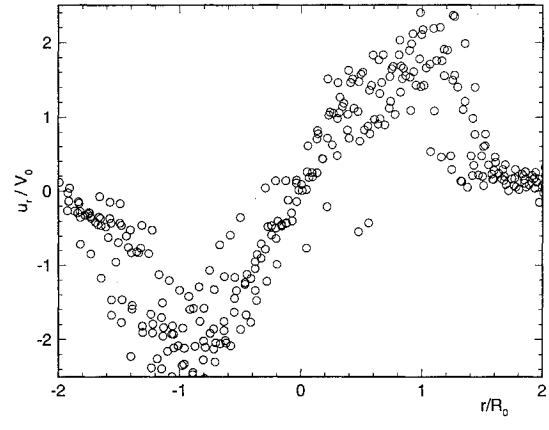

Fig. 8 Horizontal velocity along the bottom row of vectors in the baseline case; seven events overlaid.

values of vorticity generally are associated with the ring vortex. In Fig. 6a, two additional regions of high vorticity are observed near the centerline at altitudes of $0.2R_0$ and $1.3R_0$. The first region (at $0.2R_0$) corresponds to fast-moving downflow that is forced to turn due to the presence of the horizontal surface. The second region, which is particular to this event, corresponds to the shear layer between the strong downdraft near the centerline and slow-moving ambient fluid forced into the downdraft column by the vortex ring; see Fig. 2a. At $T/T_0 = 6.06$, vorticity within the ring core has increased slightly due to the stretching of the vortex ring. Also, regions of negative vorticity associated with secondary vortices are observed downstream of the primary ring. Figure 6c shows vorticity contours at $T/T_0 = 7.16$. The secondary vortices have become stronger and are swept upward by the primary vortex. The vorticity within the primary core, however, has not intensified noticeably. This is because the vortex core continues to grow by diffusion and entrainment of fluid, and also because it loses circulation to the secondary vortices. The peak value of vorticity (nondimensionalized by T_0) is approximately 16 between T/T_0 of 6.06 and 8.26. The uncertainty interval in the computed vorticity values due to uncertainty in the velocity measurements is about ± 1.

B. Event-to-Event Variations

The primary vortex structure just described is present consistently in the simulations studied, although its position at a given time varies slightly between events. The radial position of the vortex ring typically may vary by $\pm 0.1R_0$. To quantify the variations, we have plotted the instantaneous vertical and horizontal velocity profiles for a number of events in Figs. 7 and 8. Figure 7 shows PIV measurements of vertical velocities near the centerline of seven microbursts at $T/T_0 = 6.06$. Figure 8 shows horizontal velocity measurements near the surface, also in seven events, at $T/T_0 = 6.06$. In Fig. 8, the data points correspond to the bottom row of vectors in fields such

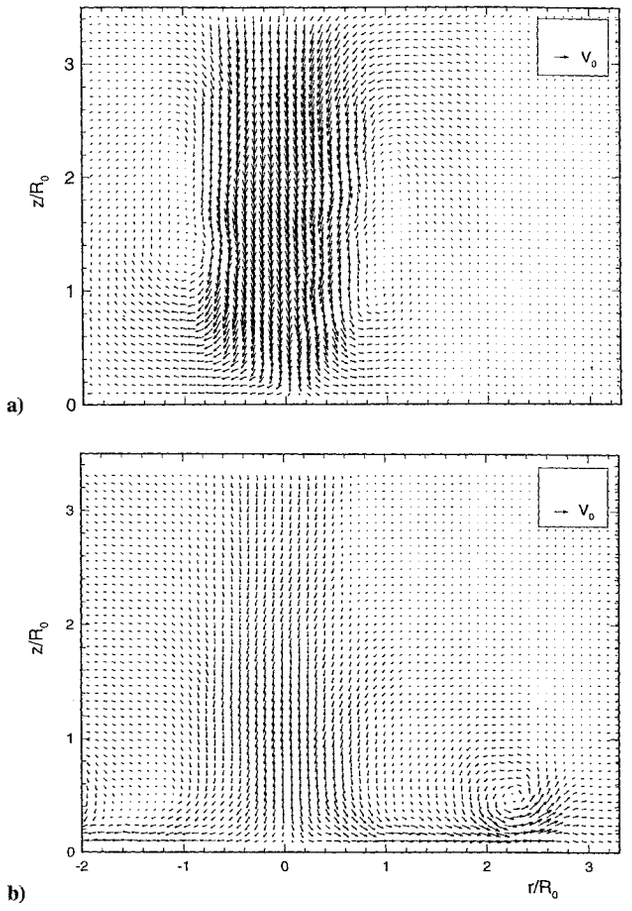

Fig. 9 Ensemble-averaged vector plots for the baseline case; times T/T_0 after release: a) 4.96 and b) 8.26.

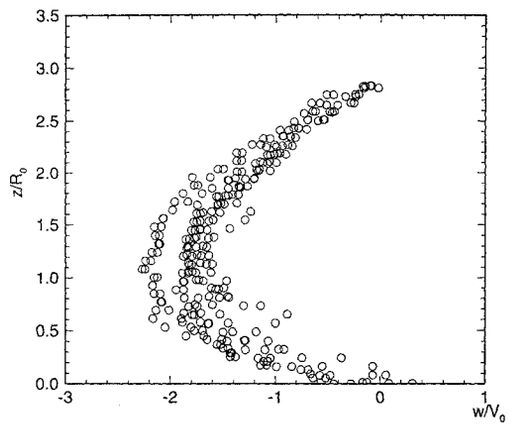

Fig. 10 Vertical velocity from the two columns closest to the centerline; four events overlaid, $H_0/R_0 = 2.86$.

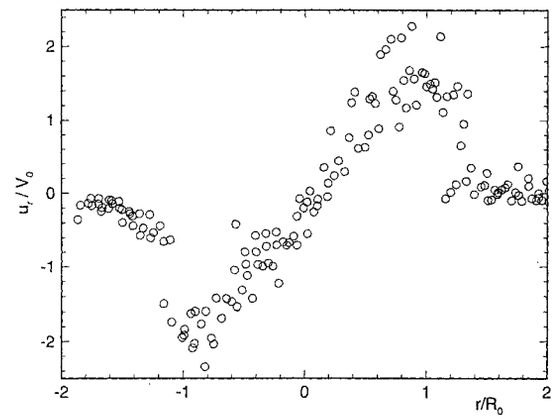

Fig. 11 Horizontal velocity along the bottom row of vectors; four events overlaid, $H_0/R_0 = 2.86$.

as the one in Fig. 2b. Both Figs. 7 and 8 show consistent behavior among the simulations studied. The scatter in Fig. 8 is expected given the azimuthal variations discussed in the preceding section.

Figures 9a and 9b display ensemble-averaged velocity fields at T/T_0 of 4.96 and 8.26. The velocity fields, averaged over 10 events, show characteristics similar to the corresponding instantaneous plots. As one would expect, the averaged plots are more axisymmetric and do not contain the small-scale shear instabilities present in the instantaneous plots. The persistence of the large structures after the averaging process, however, shows the repeatability and consistent behavior of the flow. In Fig. 9a, a second vortex ring trails the primary ring at an altitude of $2R_0$. This structure is much weaker than the primary ring and does not induce large velocities. Nevertheless, it does generate fluctuations in both vertical and horizontal velocities once it reaches the surface.

C. Effect of Initial Geometry

To study the effect of initial release height, we conducted a series of experiments with $H_0 = 2.86R_0$. The measurements for this case have been performed within vertical cross sections only. The evolution of the flow for this case is discussed in more detail in Ref. 29. Figures 10 and 11 show profiles of vertical velocity near the centerline and horizontal velocity near the surface, respectively. These measurements, taken at $T/T_0 = 4.96$, are comparable to Figs. 7 and 8 for the larger release height. The measurements indicate that the evolution of the flow after the downdraft has reached the ground is unaffected by the initial release height. This supports the work of Lundgren et al.[20] who found the behavior of microbursts to be approximately independent of the initial release height. Lundgren et al.[20] and Yao[28] explain that the circulation develops rapidly reaching a constant value while the microburst is aloft. After this point, the vortex propagates downward with nearly constant strength and velocity. Thus, as long as the initial height of the downburst parcel is sufficient for the circulation to develop fully before the parcel reaches the ground, the subsequent motion will be similar. Figure 10 shows that for $H_0 = 2.86R_0$ the peak vertical velocities are slightly lower than in the baseline case. This implies that this initial release height may be close to a lower limit for the circulation to reach its asymptotic value before impacting the surface. Because of either low cloud bases or low melting levels, the circulation may not have sufficient time to fully develop in certain atmospheric microbursts. Thus, detailed study of experimental cases with even lower release heights could be desirable.

The cylindrical containers of Lundgren et al.[20] and our baseline cylinder have aspect ratios of approximately one. Thus, the volumes have only one significant length scale. To determine the applicability of the scaling law when a second length scale is present, a series of measurements were made using a cylindrical container with the same inside diameter as the baseline case but with a height of 131 mm (aspect ratio of about 2). The equivalent spherical radius of this cylinder is 45.2 mm. The resulting scaled vertical and horizontal velocities for this case are similar to those for the baseline cylinder, but the peak velocities are sustained for longer times. Also, the radial velocity profiles near the surface display different characteristics. Figure 12 shows measurements of radial velocity at a height of $0.08R_0$ above the surface. The data are from ensemble-averaged vector plots in the vertical plane averaged over five events. The times shown correspond to time units after the downdraft reaches the surface. In Fig. 12, the velocity profiles shortly after touchdown are similar to those for the baseline case. By 2.5 time units after touchdown, however, two distinct peaks are present in the velocity profile. This is because the velocity increases radially outward from the stagnation point reaching a peak. Beyond the first peak, the velocity decays due to radial expansion, as in a steady wall jet. The second peak corresponds to the region of high radial velocity beneath the leading vortex ring. For the baseline cylinder, most of the heavy fluid resides in the primary vortex core, and due to the absence of additional trailing fluid, no inner peak appears in the profile.

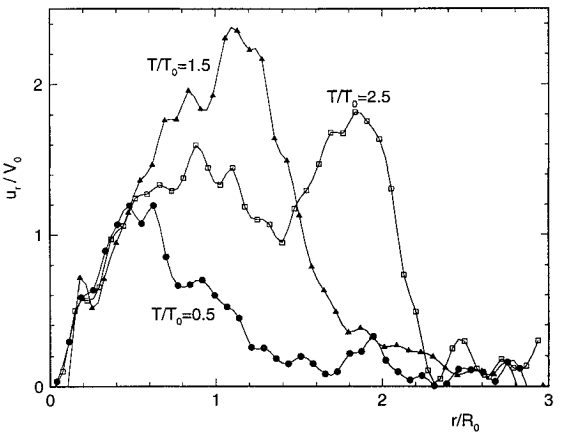

Fig. 12 Horizontal velocity along the bottom row of vectors; ensemble average of five events, R_0 = 45.2 mm.

D. Comparison with Actual Microburst Events

To compare the experimentally simulated microbursts with atmospheric ones, we first need to estimate length and time scales for each atmospheric microburst. Since only a limited amount of observational information on the June 30, 1982, downburst is available, we estimate the length and time scales for this event based on Proctor's simulation.[15,19] The length scale R_0 is estimated to be 1300 m, based on the radius of the downdraft region (Ref. 19, Table 6). This length scale puts the initial height of our downburst parcel at 4.9 km above ground level. Although the cloud base was at 2 km on this date, Doppler radar analyses showed significant downdrafts above the cloud base, and the origin height of the downdrafts was estimated to be at 4–6 km (Ref. 34).

The peak downward vertical acceleration (Dw/Dt) of the June 30 downburst was estimated from Proctor (Ref. 15, Fig. 3) to be 0.065 m/s^2. Neglecting the vertical pressure gradient, the vertical momentum equation can be written as approximately

$$\frac{Dw}{Dt} \approx -g\frac{\Delta\rho}{\rho}$$

where $g\Delta\rho/\rho$ is the total buoyancy force. In an atmospheric microburst, this force results from a combination of condensate loading and lower temperatures within the downburst. Estimating this buoyancy force and substituting it into the expression for time scale in Sec. II, we determine a time scale of 140 s and a corresponding velocity scale of 9.3 m/s.

A comparison of the observed, numerically modeled, and scaled experimental values is shown in Table 1. The values of the experimental parameters compare well with both the observed quantities and Proctor's simulations with the exception of the peak downward velocity, which is significantly larger in the experimental microburst. We believe the cause for this discrepancy is that the atmospheric microburst has a much lower acceleration above the cloud base and experiences intense acceleration only after it enters the dry adiabatic layer below the cloud base. The experimental microburst has an approximately uniform acceleration during its descending phase and, thus, attains larger vertical velocities.

Using the estimated time scale of 140 s, the maximum value of vorticity in the experimental vortex core scales to 0.11 s^{-1} in the context of this atmospheric microburst. This compares well with the computed values of 0.1–0.14 s^{-1} by Proctor.[15] As already mentioned, in the experimental microburst, the growth of the vortex core and loss of circulation to the wall mitigate the increase in vorticity due to stretching.

The microburst-producing storm on July 11, 1988, was quite complex and responsible for multiple microbursts with different intensities. Simulating the detailed characteristics of such microbursts is obviously beyond the capabilities of our simple model. As mentioned before, however, we are interested in the dynamics of the outflow once the downdraft has reached the surface. Also, the most intense of these microbursts was relatively axisymmetric near the ground at the time of peak intensity. For this microburst, we estimate a length scale of 1200 m based on the area of the downdraft region.[35] From Campbell,[36] the distance between peak outflow velocities is expanding at 8.5 m/s between 2210 and 2213 MDT, the time of peak velocity differential. Comparing this with an expansion rate of $1V_0$ for our laboratory microburst, we estimate a velocity scale of 8.5 m/s for this microburst. Thus, the simulated microburst contains a peak velocity differential of 37 m/s over a distance of 2.9 km. This compares well with the observed maximum velocity differential of 35–40 m/s. Maximum outflow velocities in the experimental microburst are 21 m/s with instantaneous peaks as high as 26 m/s. The peak vertical velocities in the simulated microburst are about 21 m/s and occur at 900 m. This is significantly higher than the observed peak of 13 m/s during the actual event[35]; however, the difference is much smaller near the surface. At an altitude of 190 m ($0.15R_0$), the downdraft velocity is approximately $0.6V_0$ or 5 m/s in the simulated microburst (see Fig. 7), which is close to an observed maximum downdraft of 4.5 m/s at 2210 MDT.[35] These comparisons imply that the near-ground microburst flowfields are simulated realistically by the experimental model.

Table 1 Comparison of experimental, TASS, and observed parameters for June 30, 1982, microburst

Parameter	Experiment	Observation	TASS
U_{max} m/s	21 ave., 29 peak	17	21
Diameter at U_{max}, m	3100	3600	3200
Outflow depth, m	650	250–750	350–750
W_{min}, m/s	−23	−15	−12
Height of W_{min}, m	950	750–1000	600–750
Propagation of front, m/s	5.6		6

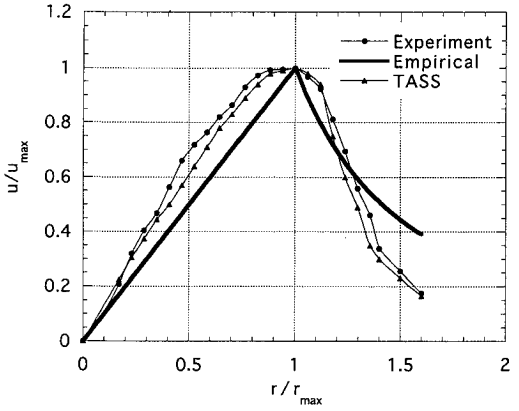

Fig. 13 Comparison of radial velocity profiles for the experimental microburst, TASS model, and an empirical model proposed by Hjelmfelt.[38]

Profiles of radial velocity vs radius from experimental microbursts are compared with profiles from the axisymmetric TASS model[37] and an empirical model from Hjelmfelt[38] in Fig. 13. The experimental profile represents the average of three events at $T/T_0 = 6.06$. Velocity is normalized by maximum outflow velocity, and radius is normalized by radius of maximum velocity. The empirical model predicts that the outflow velocity increases linearly with the scaled distance r from the microburst center and then drops off as $1/r^2$. The decay beyond the peak is much more rapid than that of a steady axisymmetric wall jet in which the velocity drops off with $1/r$. The experimental model simulates this characteristic quite well. Also, the profile from the experimental model is very similar to the profile from the TASS model. This implies that the large difference in Reynolds number between the experimental and the atmospheric microburst does not affect the shape of the outflow profile significantly.

The F factor is a nondimensional parameter that quantifies the effect of wind on the energy state of an aircraft. For nearly level flight, the F factor can be written approximately as

$$F \approx \frac{V_G}{g}\frac{\partial u}{\partial x} - \frac{w}{V_A}$$

where $\partial u/\partial x$ is the rate of change in horizontal velocity along the

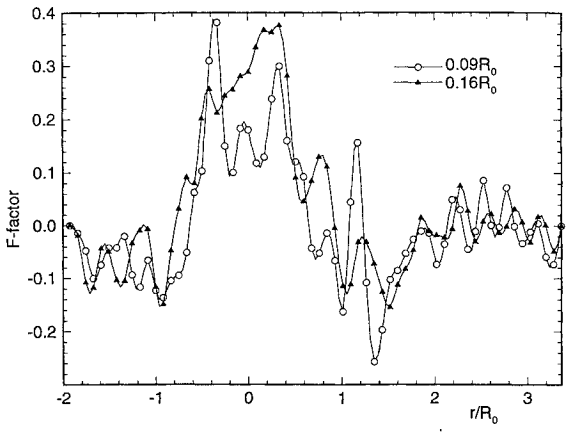

Fig. 14 *F* factor along horizontal paths at two different altitudes scaled to July 11, 1988, microburst.

flight path, u and w are the horizontal and vertical wind components, and V_A and V_G are the aircraft airspeed and ground speed, respectively. A positive F factor may be due to either an increasing horizontal wind along the aircraft flight path or a downdraft and is considered to be performance deteriorating. Conversely, a negative F factor can be caused by a decreasing wind or an updraft and is performance improving.

Figure 14 shows the local F factor computed along horizontal paths within an experimental microburst at $T/T_0 = 6.06$. The data are scaled to the July 11, 1988, microburst, and the two heights shown correspond to altitudes of 110 m and 195 m. Because of comparable length and velocity scales, the results are very similar for the June 30, 1982, microburst. The airspeed V_A is assumed to be 75 m/s (typical approach speed for jetliners). The term $\partial u/\partial x$ is obtained by the central difference method using the neighboring measurements at each point. At this time, the vortex core is located at about $1.2R_0$ from the center of the microburst. The figure shows negative values of F factor downstream of the vortex ring. This is due to the increasing headwind as the aircraft initially enters the microburst and the decreasing tailwind as the aircraft leaves the microburst. The region inside the vortex ring generally corresponds to high values of the F factor. This is due to the decreasing headwind, downdraft, and increasing tailwind within this region. Peak values of the F factor in the experimental microburst are as high as 0.39 near the ground. Peak values measured by aircraft that encountered the July 11, microburst were as high as 0.23. These aircraft, however, did not fly through the center of the microburst nor did they encounter it along the axis of maximum velocity change. The local variations in the plotted F factor appear similar to those obtained from aircraft flight recorder data (Ref. 27, Fig. 20). The maximum 1-km averaged F factor determined by the TASS model was 0.243. We did not attempt averaging our values over a certain range; however, this appears very close to our results.

V. Summary and Conclusions

The experimentally simulated flow possesses many of the dynamic characteristics observed in isolated atmospheric microbursts. PIV results show that the leading edge of the falling fluid rolls up into a vortex ring before the downdraft reaches the surface. The value of nondimensional circulation generated by the descending fluid ranges between 5 and 6 and compares well with that found numerically by Lundgren et al.[20] Horizontal velocities increase rapidly as the downdraft impacts the surface. The largest horizontal velocities ($2.5V_0$) occur within one time unit after touchdown. Microbursts are most dangerous at this time because both large gradients in horizontal velocity and large downdraft velocities are present. Both horizontal and vertical velocities decay as the microburst expands radially. Secondary vortices ahead of the primary ring tend to increase the height of the outflow and retard the propagation of the burst front. The primary vorticity increases only slightly as the vortex ring expands. Apparently, loss of circulation to the secondary vortices and the growth of the primary vortex core inhibit the intensification of vorticity through stretching.

Measurements within horizontal cross sections reveal significant azimuthal variations in the flow. These variations explain the large scatter in radial velocity measurements obtained within vertical cross sections in different events. The horizontal velocity fields are also useful in providing an average outflow velocity profile. The outflow profiles show a rapid rise in velocity near the leading edge of the microburst, which would appear as a sudden rise in airspeed to aircraft penetrating the microburst. The largest velocities, which occur at $0.05R_0$ above the surface, decay gradually with increasing altitude.

Comparisons of vertical and horizontal velocity profiles from different events show good repeatability among the events studied. Experiments with a lower release height yield results similar to the baseline case. Thus, as long as the initial height is sufficient for the circulation to develop fully before the downburst reaches the ground, the subsequent motion after impact will be similar. Measurements made using a taller cylinder show that the outflow profile develops a second peak due to the presence of additional heavy fluid upstream of the main vortex ring.

The experimental results were compared with data from two atmospheric microbursts. Scaled parameters, such as the peak outflow velocity, location of the peak outflow, outflow depth, updrafts and downdrafts within the burst front, and the overall evolution of the flow agree well with both observed atmospheric and TASS-simulated quantities. The peak downdraft velocity, however, is larger in the experimental microburst where the peak downward and outflow velocities are approximately the same. This is in good agreement with the description of an average microburst where the peak outflow and downdraft velocities are both about 12 m/s (Ref. 32). In the two microbursts discussed, the peak downdraft velocities are smaller than the peak outflow velocities. This is most likely due to complex meteorological factors, which are absent in our model. The F-factor computations show that hazardous regions exist upstream of the primary vortex core with the maximum near the center of the downburst. Local peaks as high as 0.39 are present in the F-factor measurements.

The experimental model contains the dominant driving force, developing boundary layer, large- and small-scale instabilities, and three-dimensional properties expected in atmospheric microbursts. Also, the results match well with existing data on large-scale atmospheric features. Therefore, we expect that the detailed evolving normalized velocity fields measured in the experimental flow can be used for the development and testing of improved detection algorithms required for ground-based and airborne microburst sensing systems.

Acknowledgment

This work was sponsored by the National Science Foundation under Grant CTS-9209948.

References

[1]Fujita, T. T., "Microbursts as an Aviation Wind Shear Hazard," *AIAA 19th Aerospace Sciences Meeting* (St. Louis, MO) AIAA, New York, 1981, p. 9 (AIAA Paper 81-0386).

[2]Fujita, T. T., *The Downburst*, Univ. of Chicago Press, Chicago, IL, 1985, p. 122.

[3]Fujita, T. T., *DFW Microburst*, Univ. of Chicago Press, Chicago, IL, 1986, p. 154.

[4]Elmore, K. L., McCarthy, J., Frost, W., and Chang, H. P., "A High Resolution Spatial and Temporal Multiple Doppler Analysis of a Microburst and Its Application to Aircraft Flight Simulation," *J. Climate Appl. Meteor.*, Vol. 25, 1986, pp. 1398–1425.

[5]Fujita, T. T., "Objectives, Operation, and Results of Project NIMROD," *11th Conference on Severe Local Storms* (Kansas City, KS), American Meteorological Society, 1979, pp. 259–266.

[6]McCarthy, J., Wilson, J. W., and Fujita, T. T., "The Joint Airport Weather Studies Project," *Bulletin of the American Meteorological Society*, Vol. 63, 1982, pp. 15–22.

[7]McCarthy, J., and Wilson, J. W., "The Classify, Locate and Avoid Wind Shear (CLAWS) Project at Denver's Stapleton International Airport: Operational Testing of Terminal Weather Hazard Warnings with an Emphasis on Microburst Wind Shear," *2nd International Conference on Aviation Weather System* (Boston, MA), American Meteorological Society, 1985, pp. 247–256.

[8]Dodge, J., Arnold, J., Wilson, G., Evans, J., and Fujita, T., "The Cooperative Huntsville Meteorological Experiment (COHMEX)," *Bulletin of the American Meteorological Society*, Vol. 67, 1986, pp. 417–419.

[9]Wolfson, M. M., "The FLOWS Automatic Weather Station Network," *Journal of Atmospheric and Oceanic Technology*, Vol. 6, 1989, pp. 307–326.

[10]Wakimoto, R. M., "Forecasting Dry Microburst Activity over the High Planes," *Monthly Weather Review*, Vol. 113, 1985, pp. 1131–1143.

[11]Roberts, R. D., and Wilson, J. W., "A Proposed Nowcasting Procedure Using Single-Doppler Radar," *Journal of Applied Meteorology*, Vol. 28, 1989, pp. 285–301.

[12]Caplan, S. J., Bedard, A. J., and Decker, M. T., "The 700-500 mb Lapse Rate as an Index of Microburst Probability: An Application for Thermodynamic Profilers," *Journal of Applied Meteorology*, Vol. 29, 1990, pp. 680–687.

[13]Srivastava, R. C., "A Simple Model of an Evaporatively Driven Downdraft: Application to a Microburst Downdraft," *Journal of Atmospheric Sciences*, Vol. 42, 1985, pp. 1004–1023.

[14]Srivastava, R. C., "A Model of Intense Downdrafts Driven by the Melting and Evaporation of Precipitation," *Journal of Atmospheric Sciences*, Vol. 44, 1987, pp. 1752–1773.

[15]Proctor, F. H., "Numerical Simulation of an Isolated Microburst. Part I: Dynamics and Structure," *Journal of Atmospheric Sciences*, Vol. 45, 1988, pp. 3137–3160.

[16]Droegemeier, K. K., "Simulation of Microburst Vorticity Dynamics," *15th Conference on Severe Local Storms* (Baltimore, MD), American Meteorological Society, 1988.

[17]Anderson, J. R., Droegemeier, K. K., and Wilhelmson, R. B., "Simulation of the Thunderstorm Subcloud Environment," *14th Conference on Severe Local Storms* (Indianapolis, IN), American Meteorological Society, 1985, pp. 147–150.

[18]Droegemeier, K. K., and Wilhelmson, R. B., "Numerical Simulation of Thunderstorm Outflow Dynamics. Part I: Outflow Sensitivity Experiments and Turbulence Dynamics," *Journal of Atmospheric Sciences*, Vol. 44, 1987, pp. 1180–1210.

[19]Proctor, F. H., "Numerical Simulation of an Isolated Microburst. Part II: Sensitivity Experiments," *Journal of Atmospheric Sciences*, Vol. 46, 1989, pp. 2143–2165.

[20]Lundgren, T. S., Yao, J., and Mansour, N. N., "Microburst Modelling and Scaling," *Journal of Fluid Mechanics*, Vol. 239, 1992, pp. 461–488.

[21]Turner, J. S., "Buoyant Vortex Rings," *Proceedings of the Royal Society of London*, Vol. A239, 1957, pp. 61–75.

[22]Scorer, R. S., "Experiments on Convection of Isolated Masses of Buoyant Fluid," *Journal of Fluid Mechanics*, Vol. 2, 1957, pp. 583–594.

[23]Simpson, J. E., "A Comparison Between Laboratory and Atmospheric Density Currents," *Quarterly of the Journal of the Royal Meteorological Society*, Vol. 95, 1969, pp. 758–765.

[24]Simpson, J. E., "Effects of the Lower Boundary on the Head of a Gravity Current," *Journal of Fluid Mechanics*, Vol. 53, 1972, pp. 759–768.

[25]Simpson, J. E., and Britter, R. E., "The Dynamics of the Head of a Gravity Current Advancing over a Horizontal Surface," *Journal of Fluid Mechanics*, Vol. 94, 1979, pp. 477–495.

[26]Huppert, H. E., and Simpson, J. E., "The Slumping of Gravity Currents," *Journal of Fluid Mechanics*, Vol. 99, 1980, pp. 785–799.

[27]Proctor, F. H., and Bowles, R. L., "Three-Dimensional Simulation of the Denver 11 July, 1988, Microburst-Producing Storm," *Meteorological Atmospheric Physics*, Vol. 49, 1992, pp. 107–124.

[28]Yao, J., "Experiments on Microbursts," Ph.D. Thesis, Univ. of Minnesota, Minneapolis, MN, 1993, p. 159.

[29]Alahyari, A., and Longmire, E. K., "Particle Image Velocimetry in a Variable Density Flow: Application to a Dynamically Evolving Microburst," *Experiments in Fluids*, Vol. 17, 1994, pp. 434–440.

[30]Widnall, S. E., and Sullivan, J. P., "On the Stability of Vortex Rings," *Proceedings of the Royal Society of London Series A: Mathematical and Physical Sciences*, Vol. 332, 1973, pp. 335–353.

[31]Saffman, P. G., "The Number of Waves on Unstable Vortex Rings," *Journal of Fluid Mechanics*, Vol. 84, 1978, pp. 625–639.

[32]Wilson, J. W., Roberts, R. D., Kessinger, C., and McCarthy, J., "Microburst Wind Structure and Evolution of Doppler Radar for Airport Wind Shear Detection," *Journal of Climate Applied Meteorology*, Vol. 23, 1984, pp. 898–915.

[33]Cerra, A. W., and Smith, C. R., "Experimental Observation of Vortex Ring Interaction with the Fluid Adjacent to a Surface," Dept. of Mechanical Engineering and Mechanics, Rept. FM-4, Lehigh Univ., Bethlehem, PA, 1983, p. 178.

[34]Kessinger, C., Parsons, D. B., and Wilson, J. W., "Observation of a Storm Containing Misocyclones, Downbursts, and Horizontal Vortex Circulation," *Monthly Weather Review*, Vol. 116, 1988, pp. 1959–1982.

[35]Elmore, K. L., Politovich, M. K., and Sand, W. R., "The 11 July Microburst at Stapleton International Airport, Denver, Colorado," *Windshear Case Study: Denver, Colorado, July 11, 1988*, Final Rept., DOT/FAA/DS-89/19, Federal Aviation Administration, 1989, Appendix 5 (available from National Technical Information Service).

[36]Campbell, S., *Windshear Case Study: Denver, Colorado, July 11, 1988*, Final Rept., DOT/FAA/DS-89/19, Federal Aviation Administration, MIT Lincoln Lab. Rept., 1989, Appendix 4 (available from National Technical Information Services).

[37]Byrd, G. P., Proctor, F. H., and Bowles, R. L., "Evaluation of a Technique to Quantify Microburst Windshear Hazard Potential to Aircraft," *Proceedings of the 29th Conference on Decision and Control*, 1990, pp. 689–694.

[38]Hjelmfelt, M. R., "Structure and Life Cycle of Microburst Outflows Observed in Colorado," *Journal of Applied Meteorology*, Vol. 27, 1988, pp. 900–927.